

An unstructured-mesh finite-volume MPDATA for compressible atmospheric dynamics

Christian Kühnlein^a, Piotr K. Smolarkiewicz^a

^a*European Centre for Medium-Range Weather Forecasts, Shinfield Park, Reading, RG2 9AX, United Kingdom*

Abstract

An advancement of the unstructured-mesh finite-volume MPDATA (Multidimensional Positive Definite Advection Transport Algorithm) is presented that formulates the error-compensative pseudo-velocity of the scheme to rely only on face-normal advective fluxes to the dual cells, in contrast to the full vector employed in previous implementations. This is essentially achieved by expressing the temporal truncation error underlying the pseudo-velocity in a form consistent with the flux-divergence of the governing conservation law. The development is especially important for integrating fluid dynamics equations on non-rectilinear meshes whenever face-normal advective mass fluxes are employed for transport compatible with mass continuity—the latter being essential for flux-form schemes. In particular, the proposed formulation enables large-time-step semi-implicit finite-volume integration of the compressible Euler equations using MPDATA on arbitrary hybrid computational meshes. Furthermore, it facilitates multiple error-compensative iterations of the finite-volume MPDATA and improved overall accuracy. The advancement combines straightforwardly with earlier developments, such as the nonoscillatory option, the infinite-gauge variant, and moving curvilinear meshes. A comprehensive description of the scheme is provided for a hybrid horizontally-unstructured vertically-structured computational mesh for efficient global atmospheric flow modelling. The proposed finite-volume MPDATA is verified using selected 3D global atmospheric benchmark simulations, representative of hydrostatic and non-hydrostatic flow regimes. Besides the added capabilities, the scheme retains fully the efficacy of established finite-volume MPDATA formulations.

Keywords: finite-volume scheme, unstructured mesh, nonoscillatory scheme, semi-implicit, compressible Euler equations, atmospheric flows

1. Introduction

Simulation of atmospheric flows is challenging due to the multifaceted nonlinear processes and tremendous range of scales involved. Notwithstanding the achievements made over the last decades [1], weather and climate prediction still face the formidable task to resolve important circulations and multi-scale interactions, most notably those associated with convective clouds and orography. Generally, weather and climate prediction are confronted with high-Reynolds low-Mach number rotating stably-stratified flows that are described on all scales by the compressible Euler equations. Efficiently integrating the Euler equations despite the omnipresence of fast acoustic and buoyant modes, while accurately predicting the perturbations about fundamental large-scale balances, guides the design of atmospheric models.

Unstructured computational meshes offer great flexibility for implementing variable, adaptive resolution in numerical models. The technique facilitates locally finer mesh spacings in sensitive regions, such as along coastlines, in mountainous areas, or the tropics, and relatively coarser spacings elsewhere. Unstructured meshes are also highly relevant for efficient integration of the governing equations in the spherical

Email addresses: christian.kuehnlein@ecmwf.int (Christian Kühnlein), piotr.smolarkiewicz@ecmwf.int (Piotr K. Smolarkiewicz)

domains underlying global prediction systems. For the global configurations the technique provides ample freedom for implementing various quasi-uniform resolution meshes that circumvent the stiffness from the converging meridians towards the poles of the classical regular longitude-latitude grids. The combination of efficient quasi-uniform global meshes and possible adaptivity represents a powerful approach for modelling atmospheric flows. Finite-volume (FV) discretisation methods can be effectively applied with arbitrary unstructured meshes, and also offer the intrinsic advantages of fully conservative transport and local computations on compact stencils. Towards more realistic high-resolution applications in weather and climate, FV methods permit fairly straightforward coupling to existing sub-grid scale physics parametrisations developed for traditional grid-point methods.

MPDATA refers to a class of nonoscillatory forward-in-time (NFT) high-resolution numerical schemes for the advective terms in flux-form formulations of fluid equations. MPDATA originated in the 1980's as a finite-difference (FD) scheme for simulation of atmospheric clouds [2]. The basic principle of MPDATA is most suitably described as an iterated upwind (*alias* donor cell) scheme: The initial iteration represents the first-order accurate upwind scheme with the advective velocity given by the physical flow. Subsequent iterations are also based on the upwind scheme, but the updated field is advected with a properly defined pseudo-velocity designed to compensate to selected order (typically second) the spatial and temporal truncation errors of the previous iteration. The resulting scheme is at least second-order accurate in time and space, fully multidimensional and conservative. Due to the consistent application of the upwind differencing, MPDATA retains the characteristic features of a relatively small phase error and strict sign preservation of the transported field. Sign preservation (i.e. positivity) is imperative and conservation is highly desirable for the transport of moisture and chemistry variables in atmospheric models. In addition, positivity of flux-form schemes is sufficient for the nonlinear stability [3].

Over the subsequent decades MPDATA evolved into a family of integration schemes for systems of generalised transport equations while targeting conservation laws of atmospheric dynamics on co-located meshes. Consistently expanding the realm of the second-order MPDATA for advection to general conservation laws relies on a rigorous extension of the underlying forward-in-time (FT) truncation error analysis to arbitrary right-hand-sides [4, 5, 6]. Concomitantly, numerous advancements for advective transport increased the range of application of MPDATA. One example is the nonoscillatory option [7, 3] to ensure solution monotonicity away from zero values where the sign-preserving mechanism is not effective. Another example is the infinite-gauge variant [8, 5, 6] that represents an asymptotic form of MPDATA (in the limit of an infinite constant background) which is not sign-preserving but maintains the solution slope at sign transitions for variable-sign fields. The latter property and favourable efficacy [8] make the infinite-gauge a useful option for the transport of general fields such as velocity components or temperature perturbations in flow solvers—the infinite-gauge is standardly applied with the nonoscillatory option. Finally, when employed in the context of flow solvers, the nonoscillatory MPDATA becomes highly effective as it qualifies for implicit large-eddy simulation (ILES) of high-Reynolds number atmospheric flows [9, 10, 11, 12, 13]. An ILES option is of significant practical interest, and this applies particularly to simulations with complex meshes where the flow regularisation by means of explicit sub-grid scale turbulence models can be involving [14].

Originally, MPDATA was formulated using FD methods on structured rectilinear grids [2, 5]. The FD-MPDATA can be combined with generalised curvilinear coordinates to accommodate complex boundaries such as orography [8, 15, 16] or to implement adaptive moving meshes [17, 18]. Given the success of the FD-MPDATA (see [19] for a comprehensive list of references), a significant later advancement is an edge-based FV formulation of MPDATA for fully unstructured meshes [20, 3]. In contrast to the FD-MPDATA, the FV-MPDATA enables arbitrary meshes consisting of various cell shapes, yielding greater flexibility and added capabilities for complex domains and mesh adaptivity [21, 22, 12, 13]. The FD- and FV-MPDATA feature applicability for a broad variety of geophysical/astrophysical [23, 24, 25] and engineering [21, 26] problems.

MPDATA-based flow solvers come in various flavours depending on the focus of application. Historically, MPDATA grew out of the area of small- and meso-scale nonhydrostatic atmospheric dynamics, and was primarily employed to solve soundproof (incompressible Boussinesq, anelastic, pseudo-incompressible) equations on structured grids [5, 27, 19], with later generalisation to unstructured meshes [28, 29]. The underlying soundproof integration schemes have a number of favourable features. Besides advantages of large

time steps due to the absence of acoustic modes, solving directly for primitive variables (e.g. physical velocity components) while satisfying their conservation laws (i.e. momentum) enables the Lagrangian-Eulerian congruence [4] and facilitates design of semi-implicit time stepping [30, 19]. This contrasts with solving for conserved, density-type, variables standard in high-Mach number gas dynamics [26] or free-surface incompressible flows [31]. Solving for conserved variables impedes design of semi-implicit schemes due to nonlinearities arising from weighting of the primitive variables with density.

Recently, the MPDATA-based integration schemes for soundproof equations were extended to the compressible Euler equations for low-Mach number flows [25]. One particular feature of the developed integration schemes is the 3D implicit temporal treatment of buoyant and acoustic modes—resulting in unconditional stability, and hence large time steps (equivalent to soundproof models), with respect to these fast processes. The reduced soundproof (anelastic, pseudo-incompressible) equations were shown to be significantly less accurate for planetary scales (see Section 4.1 in [25]), which favours the compressible Euler equations for global all-scale atmospheric modelling. While [25] focused on structured rectilinear grids, the present work extends the earlier developments to arbitrary hybrid computational meshes. The key aspect is to reformulate the established FV-MPDATA [32, 3] such that it operates only on face-normal vector components to the dual cells of the unstructured mesh. The advanced FV-MPDATA straightforwardly achieves full compatibility with mass continuity, i.e. replicates the discrete compressible mass continuity equation wherever the transported field is locally constant. This compatibility is crucial for the solution monotonicity and prevents obscuring time tendencies of variables’ perturbations by the associated residual errors amplified with large constant backgrounds [18]. Moreover, the advancement facilitates multiple error-compensative iterations of the finite-volume MPDATA. The presented scheme is the basis of a novel finite-volume module (FVM) for global all-scale atmospheric flows [33].

The paper is organised as follows. Section 2 summarises the established FV-MPDATA for the integration of a homogeneous advective conservation law on unstructured meshes. Section 3 presents a truncation error analysis for the FT discretisation of a generalised transport equation of fluid dynamics. This discussion reveals alternative formulations of the FV-MPDATA for compressible atmospheric dynamics. The discrete implementation of this scheme is then presented in Section 4. Section 5 outlines the low-Mach number integration procedures for the compressible Euler equations developed in [25] and clarifies the importance of the proposed formulation for arbitrary unstructured meshes. Global atmospheric flow simulations are then utilised in Section 6 to compare the advanced FV-MPDATA to the established reference formulations for mesoscale mountain wave and baroclinic instability benchmarks. Section 7 concludes the paper.

2. Basic finite-volume MPDATA

We begin by summarising the basic FV-MPDATA for solution of the homogenous conservation law

$$\frac{\partial G\psi}{\partial t} + \nabla \cdot (\mathbf{V}\psi) = 0, \quad (1)$$

where $\psi = \psi(\mathbf{x}, t)$ is a (non-diffusive) scalar field assumed nonnegative at time $t = 0$. The field $\mathbf{V} = G\dot{\mathbf{x}}$ represents the advector, where $\dot{\mathbf{x}}$ is the contravariant velocity in the underlying coordinate system. The symbol G typically incorporates geometric and physical aspects by means of the Jacobian of coordinate transformations and the fluid density, respectively. We assume $G(\mathbf{x})$ to be time-independent in the present section; a more general case is considered in the subsequent sections.

Employing the Gauss divergence theorem $\int_{\Omega} \nabla \cdot (\mathbf{V}\psi) = \int_{\partial\Omega} \psi \mathbf{V} \cdot \mathbf{n}$, the discrete FT integral of (1) over an arbitrary computational cell is written as [20, 3]

$$\psi_i^{n+1} = \psi_i^n - \frac{\delta t}{G_i \mathcal{V}_i} \sum_{j=1}^{l(i)} F_j^\perp S_j, \quad (2)$$

where the index i refers to the node representing the cell with dual volume \mathcal{V}_i , and this cell i is connected via $l(i)$ edges to its immediate neighbouring cells represented by nodes j ; S_j describes both the face of the

dual volume and its surface area; see the schematic provided in Fig. 1. The n and $n + 1$ indices denote the time levels, and $\delta t = t^{n+1} - t^n$ the time step increment. The symbol F_j^\perp represents the mean normal flux of ψ through the surface S_j .

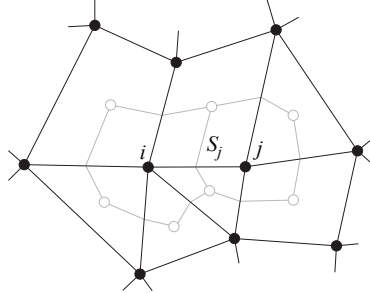


Fig. 1: Schematic of the median-dual mesh in 2D. The edge connecting nodes i and j of the primary polygonal mesh pierces, precisely in the edge centre, the face S_j shared by computational dual cells surrounding nodes i and j . Open circles represent geometrical barycentres of the primary mesh, solid black lines mark the primary mesh and grey lines indicate dual cells with control volumes \mathcal{V}_i and \mathcal{V}_j , respectively.

The first step in MPDATA represents the first-order accurate upwind scheme, which in case of (2) results in the flux F_j^\perp approximated as

$$F_j^\perp(\psi_i, \psi_j, V_j^\perp) = [V_j^\perp]^+ \psi_i + [V_j^\perp]^- \psi_j \quad (3)$$

with the normal velocity $V^\perp \equiv \mathbf{n} \cdot \mathbf{V}$ evaluated at the surface S_j , and its positive and negative parts defined as

$$[V^\perp]^+ \equiv \max[0, V^\perp], \quad [V^\perp]^- \equiv \min[0, V^\perp]. \quad (4)$$

A modified equation analysis of the scheme for the solution ψ about the time level $t^{n+1/2}$ and a point s_j along the edge connecting nodes i and j where the edge intersects the cell face S_j , shows the following form of the truncation error [3]

$$\begin{aligned} \text{Error} = & -\frac{1}{2}|V_j^\perp| \left(\frac{\partial \psi}{\partial r} \right)_{s_j}^* (r_j - r_i) + \frac{1}{2}V_j^\perp \left(\frac{\partial \psi}{\partial r} \right)_{s_j}^* (r_i - 2r_{s_j} - r_j) \\ & + \frac{1}{2}\delta t \frac{V_j^\perp}{G_j} \{\mathbf{V} \cdot \nabla \psi\}_{s_j}^* + \frac{1}{2}\delta t \frac{V_j^\perp}{G_j} \{\psi(\nabla \cdot \mathbf{V})\}_{s_j}^* + \mathcal{O}(\delta r^2, \delta t^2, \delta r \delta t), \end{aligned} \quad (5)$$

with the parametric description of the edge $r(\lambda) = r_i + \lambda(r_j - r_i)$, $\lambda \in [0, 1]$. The asterisk in lieu of the time level in the error (5) symbolises either n , $n + 1/2$, or $n + 1$, as any of these temporal positions can be considered without affecting the form or the order of the error [3]. The two $\mathcal{O}(\delta r)$ terms in (5) result from the spatial upwind differencing. The second of these describes a 'mesh-skewness' error that vanishes with an appropriate discretisation [3]; the edge-based median-dual approach illustrated in Fig. 1 represents one example assumed in the present work. The two $\mathcal{O}(\delta t)$ terms in the second line of (5) originate from the temporal decentering of the upwind scheme. In the derivation of these $\mathcal{O}(\delta t)$ terms a time derivative in the truncation error was expressed by spatial derivatives—a Cauchy-Kowalewski procedure [34] rooted in the PDE (1) [3]. Given (5), MPDATA employs a pseudo-velocity $\tilde{V}^\perp := -\psi^{-1} \times \text{Error}(\delta r, \delta t)$ in an error-compensative upwind step using the preceding upwind solution. One corrective iteration suffices for $\mathcal{O}(\delta r^2, \delta t^2)$ accuracy of the overall scheme¹. A detailed description of the implementation of (5) is provided in [3], together with a discussion of the consistency, stability and accuracy of the FV-MPDATA.

¹For example, convergence along constant Courant numbers warrants the $\mathcal{O}(\delta r^2, \delta t^2)$ accuracy of the scheme, where δr is a spatial increment.

3. MPDATA for conservation laws

The subsequent presentation discusses the MPDATA scheme for a generalised transport equation with arbitrary rhs R^Ψ

$$\frac{\partial G\Psi}{\partial t} + \nabla \cdot (\mathbf{V}\Psi) = GR^\Psi, \quad (6)$$

which accommodates typical conservation laws of many fluid dynamics problems [26, 25]; a particular example is given by the low-Mach-number integration scheme for the compressible Euler equations described in Section 5.

We follow earlier works (see [6] and references therein) and derive a two-time-level second-order-accurate MPDATA integration scheme for the generalised transport equation (6) given $\mathbf{V}(\mathbf{x}, t)$, $G(\mathbf{x}, t)$ and $R^\Psi(\mathbf{x}, t)$ are known functions to at least $\mathcal{O}(\delta t^2)$. The derivation assumes the temporal discretisation

$$\frac{G^{n+1}\Psi^{n+1} - G^n\Psi^n}{\delta t} + \nabla \cdot (\mathbf{V}^{n+1/2}\Psi^n) = (GR^\Psi)^{n+1/2}. \quad (7)$$

Expanding all fields in a second-order Taylor-series about the time level t^n results in

$$\frac{\partial G\Psi}{\partial t} + \nabla \cdot (\mathbf{V}\Psi) = GR^\Psi - \frac{\partial^2 G\Psi}{\partial t^2} \frac{\delta t}{2} - \nabla \cdot \left(\Psi \frac{\partial \mathbf{V}}{\partial t} \frac{\delta t}{2} \right) + \frac{\partial GR^\Psi}{\partial t} \frac{\delta t}{2} + \mathcal{O}(\delta t^2), \quad (8)$$

or

$$\frac{\partial G\Psi}{\partial t} + \nabla \cdot (\mathbf{V}\Psi) = GR^\Psi + \mathcal{O}(\delta t). \quad (9)$$

Differentiating (9) with respect to time gives

$$\frac{\partial^2 G\Psi}{\partial t^2} + \nabla \cdot \left(\frac{\partial \mathbf{V}}{\partial t} \Psi \right) + \nabla \cdot \left(\mathbf{V} \frac{\partial \Psi}{\partial t} \right) = \frac{\partial GR^\Psi}{\partial t} + \mathcal{O}(\delta t), \quad (10)$$

which upon insertion into (8) leads to the following modified equation of the discretisation (7)

$$\frac{\partial G\Psi}{\partial t} + \nabla \cdot (\mathbf{V}\Psi) = GR^\Psi + \nabla \cdot \left(\mathbf{V} \frac{\partial \Psi}{\partial t} \frac{\delta t}{2} \right) + \mathcal{O}(\delta t^2). \quad (11)$$

Interpretation and evaluation of the $\mathcal{O}(\delta t)$ truncation error term in (11) is typically performed by representing the temporal derivative with (9) written as

$$\frac{\partial \Psi}{\partial t} = -\frac{\Psi}{G} \frac{\partial G}{\partial t} - \frac{1}{G} \mathbf{V} \cdot \nabla \Psi - \frac{\Psi}{G} \nabla \cdot \mathbf{V} + R^\Psi + \mathcal{O}(\delta t), \quad (12)$$

which leads to the modified equation

$$\begin{aligned} \frac{\partial G\Psi}{\partial t} + \nabla \cdot (\mathbf{V}\Psi) = GR^\Psi - \nabla \cdot \left\{ \frac{\delta t}{2} \mathbf{V} \left[\frac{1}{G} (\mathbf{V} \cdot \nabla \Psi) + \frac{\Psi}{G} \left(\frac{\partial G}{\partial t} + \nabla \cdot \mathbf{V} \right) \right] \right\} \\ + \nabla \cdot \left(\mathbf{V} R^\Psi \frac{\delta t}{2} \right) + \mathcal{O}(\delta t^2), \end{aligned} \quad (13)$$

where the $\mathcal{O}(\delta t)$ error is expressed in terms of spatial derivatives of Ψ —the aforementioned Cauchy-Kowalevski procedure. Hence, a fully second-order-accurate two-time-level integration scheme can be attained by compensating in (7), to at least $\mathcal{O}(\delta t^2)$, for the error on the rhs of (13). Two distinct components of the $\mathcal{O}(\delta t)$ errors occur on the rhs of (13). The terms in the curly brackets result from the uncentred temporal differencing of the homogeneous version of (7), i.e. with $R^\Psi \equiv 0$. Consequently, these terms are associated solely with advection and represent the basis for designing advanced MPDATA advective transport

schemes below. The error term $\sim 0.5 \mathbf{V} R^\Psi \delta t$ couples advection and forcing. An effective way of compensating the $\mathcal{O}(\delta t)$ error associated with the forcing R^Ψ is by assuming $R^\Psi|^{n+1/2} = 0.5 (R^\Psi|^{n+1} + R^\Psi|^{n+1/2})$, where $R^\Psi|^{n+1}$ is known to at least $\mathcal{O}(\delta t^2)$, and advecting the auxiliary field $\tilde{\Psi}^n \equiv \Psi^n + 0.5 \delta t R^\Psi|^{n+1}$ (instead of Ψ^n alone) [4]. Moreover, the procedure of advecting $\tilde{\Psi}^n$ makes this Eulerian solution approach congruent to two-time-level semi-Lagrangian schemes [4, 5].

Common to all MPDATA formulations so far is the basic form of the modified equation given in (13), i.e. the temporal truncation error associated with advection composed in a term containing the advective derivative $\sim \mathbf{V} \cdot \nabla \Psi$ and the flow divergence $\sim \nabla \cdot \mathbf{V}$. This form is particularly beneficial when the second term in the square brackets on the rhs of (13) vanishes identically, such as in soundproof systems [25]. In the present work, we consider alternative forms to (13) for designing MPDATA. Simply rewriting (12) as

$$\frac{\partial \Psi}{\partial t} = -\frac{\Psi}{G} \frac{\partial G}{\partial t} - \frac{1}{G} \nabla \cdot (\mathbf{V} \Psi) + R^\Psi + \mathcal{O}(\delta t), \quad (14)$$

upon insertion into (11), gives

$$\frac{\partial G \Psi}{\partial t} + \nabla \cdot (\mathbf{V} \Psi) = G R^\Psi - \nabla \cdot \left\{ \frac{\delta t}{2} \mathbf{V} \left[\frac{1}{G} \nabla \cdot (\mathbf{V} \Psi) + \frac{\Psi}{G} \frac{\partial G}{\partial t} \right] \right\} + \nabla \cdot \left(\mathbf{V} R^\Psi \frac{\delta t}{2} \right) + \mathcal{O}(\delta t^2). \quad (15)$$

The modified equation (15) is mathematically equivalent to (13) but inspires a different numerical approximation. The term $\sim 0.5 \mathbf{V} R^\Psi \delta t$ is identical, and the $\mathcal{O}(\delta t)$ error terms related solely to advection are again given in the curly brackets, but here composed into a term containing the generic flux divergence $\sim \nabla \cdot (\mathbf{V} \Psi)$ and $\sim \partial G / \partial t$.

As explained in Section 2, the pseudo-velocity in the error-compensative steps of MPDATA is normal to the dual cell face $\tilde{V}^\perp := -\Psi^{-1} \times \text{Error}(\delta r, \delta t)$. The $\text{Error}(\delta r, \delta t)$ is composed of the spatial $\mathcal{O}(\delta r)$ and temporal $\mathcal{O}(\delta t)$ truncation errors of the upwind scheme. While (13) and (15) expose the temporal truncation errors, the respective spatial truncation errors associated with the upstream differencing always assume the form as given by the first two terms on the rhs of (5). The form of the $\mathcal{O}(\delta t)$ error with respect to advection in (15) turns out to be advantageous for unstructured meshes. When constructing MPDATA based on (15), the resulting pseudo-velocity operates only with normal components to the dual cell face V^\perp , as all vectors \mathbf{V} in (15) appear in connection with divergence operators. In addition, the $\mathcal{O}(\delta r)$ error terms from spatial upwind differencing also contain only face-normal components; see (5) and the discrete implementations provided in Section 4. In contrast, the MPDATA pseudo-velocity based on (13) additionally requires the full vector \mathbf{V} in order to evaluate the scalar product of the advective derivative $\sim \mathbf{V} \cdot \nabla \Psi$. In particular, for applications with $\partial G / \partial t \equiv 0$ and significant flow divergence $\nabla \cdot \mathbf{V}$, such as in gas dynamics [26], the form (15) also results in a more compact pseudo-velocity expression than (13).

The FV-MPDATA operating only on face-normal velocity components becomes especially useful in the context of the low-Mach-number semi-implicit integration scheme for the compressible Euler equations of [25], which is outlined in Section 5. An essential procedure in this integration scheme is that the MPDATA solution of the mass continuity equation, besides updating ρ , accumulates the normal mass fluxes $V^\perp \rho$ through the dual cell face used in the computation of the mass flux divergence. Subsequently, these normal mass fluxes are employed in the advective transport of all primitive variables. Consequently, FV advective transport of these primitive variables is fully compatible with the (discrete) mass continuity. Due to the nature of the FV approach—i.e. relying on the Gauss divergence theorem—no information is available for the face-tangential mass flux. Therefore, unless rectilinear grids are employed as in [25], these tangential components are missing for evaluation of the pseudo-velocity in the established FV-MPDATA formulations based on (13). Although the missing face-tangential components could in principle be estimated from normal components of surrounding cells, such an elaborate approach might significantly degrade the efficacy of the scheme. These issues are absent if the FV-MPDATA can be based on (15), because the provision of the accumulated face-normal mass fluxes from mass continuity alone is sufficient to achieve fully compatible $\delta t \mathcal{O}(\delta r^2, \delta t^2)$ accurate solutions for arbitrary meshes.

Another virtue of (15) is that it facilitates multiple error-compensative iterations of MPDATA on arbitrary meshes. Basically, one corrective step suffices for $\mathcal{O}(\delta r^2, \delta t^2)$ accuracy of MPDATA and this is what is

most often used in practice. However, multiple corrective iterations can significantly increase solution quality for certain applications with rectilinear computational grids [5], which also makes this a desirable option for arbitrary meshes. As can be seen from discrete implementations provided in Section 4, any iterations subsequent to the first corrective step involve the pseudo-velocity of the previous iteration [5]. Again, the pseudo-velocity is always normal to the dual cell face, and thus lack face-tangential components needed with (13) for non-rectilinear meshes. Therefore, the MPDATA operating solely with face-normal components is self-contained for multiple error-compensative iterations, and circumvents the problematic construction of the face-tangential components from face-normal components for each corrective iteration.

4. Implementation

Here we present the discrete implementation of the advanced FV-MPDATA following our modified equation analysis of the previous section. We consider a hybrid computational mesh, unstructured in the horizontal and structured in the vertical, which is of particular relevance to global atmospheric modelling [33]. While the unstructured horizontal mesh is an effective way to achieve quasi-uniform resolution over the surface of the sphere and optionally local mesh adaptivity, the structured grid benefits direct preconditioning of elliptic operators in the stiff vertical direction, important for efficient integration of the governing equations with implicit time stepping. The subsequently presented discrete formulae of the hybrid mesh apply to a fully unstructured mesh in 3D by simply neglecting the contributions pertaining to the structured vertical grid.

The numerical integral of the homogeneous generalised transport equation (6) with $R^\Psi \equiv 0$ can be written in the functional form as [33]

$$\begin{aligned}\Psi_{\mathbf{i}}^{n+1} &= \mathcal{A}_{\mathbf{i}}(\Psi^n, \mathbf{V}^{n+1/2}, G^n, G^{n+1}) \\ &= \chi_{\mathbf{i}}^{n+1/2} \tilde{\mathcal{A}}_{\mathbf{i}}(\Psi^n, \mathbf{V}^{n+1/2}, G^n, G^{n+1}) \\ &= \chi_{\mathbf{i}}^{n+1/2} \Psi_{\mathbf{i}}^{\mathcal{N}_\eta},\end{aligned}\tag{16}$$

where $\mathbf{i} = (k, i)$ is the vector index marking the node positions k and i of the vertical and horizontal computational mesh, respectively, and the factor

$$\chi^{n+1/2} \equiv \frac{G^n}{G^{n+1}}\tag{17}$$

results from the time-dependent $G(\mathbf{x}, t)$. Given (16), the operator $\tilde{\mathcal{A}}_{\mathbf{i}}$ iterates for $\eta = 1, \mathcal{N}_\eta$ the discrete form

$$\begin{aligned}\Psi_{k,i}^{(\eta)} &= \Psi_{k,i}^{(\eta-1)} - \frac{\delta t}{G_{k,i}^n \mathcal{V}_i} \sum_{j=1}^{l(i)} F_{k,j}^\perp \left(\Psi_{k,i}^{(\eta-1)}, \Psi_{k,j}^{(\eta-1)}, V_{k,j}^\perp{}^{(\eta)} \right) S_j \\ &\quad - \frac{\delta t}{G_{k,i}^n \delta z} \left\{ F_{k+1/2,i}^z \left(\Psi_{k,i}^{(\eta-1)}, \Psi_{k+1,i}^{(\eta-1)}, V_{k+1/2,i}^z{}^{(\eta)} \right) \right. \\ &\quad \left. - F_{k-1/2,i}^z \left(\Psi_{k-1,i}^{(\eta-1)}, \Psi_{k,i}^{(\eta-1)}, V_{k-1/2,i}^z{}^{(\eta)} \right) \right\},\end{aligned}\tag{18}$$

which formally combines a horizontal FV with a vertical flux-form FD approach [33, 35]. As in Section 2, further parameters that enter (18) are the dual cell volume \mathcal{V}_i , the dual cell face area S_j , the vertical mesh spacing δz , and the time step δt . The second term on the rhs of (18) represents the horizontal divergence of the advective upwind flux $F_{k,j}^\perp$ normal to the S_j face of the dual cell surrounding node i as

$$F_{k,j}^\perp \left(\Psi_{k,i}, \Psi_{k,j}, V_{k,j}^\perp \right) = [V_{k,j}^\perp]^+ \Psi_{k,i} + [V_{k,j}^\perp]^- \Psi_{k,j},\tag{19}$$

where positive $[V^\perp]^+$ and negative $[V^\perp]^-$ parts coincide with outflow and inflow from the i th dual cell. The third term on the rhs of (18) represents the vertical divergence of the advective upwind flux F^z through the faces of the prismatic cells

$$F_{k+1/2,i}^z \left(\Psi_{k,i}, \Psi_{k+1,i}, V_{k+1/2,i}^z \right) = [V_{k+1/2,i}^z]^+ \Psi_{k,i} + [V_{k+1/2,i}^z]^- \Psi_{k+1,i},\tag{20}$$

where here $[V^z]^+$ and $[V^z]^-$ involve Ψ from the nodes below and above, respectively. A fixed bottom-to-top orientation of the prismatic cells is assumed in the vertical, therefore positive/negative V^z at the face $k+1/2$ above the node k correspond to outflow/inflow, and vice versa at the face $k-1/2$ below node k .

For $\eta = 1$, the scheme (18) is then initialised as

$$\Psi^{(0)} \equiv \Psi^n, \quad V^{\perp(1)} \equiv V^{\perp, n+1/2}, \quad V^{z(1)} \equiv V^{z, n+1/2}, \quad (21)$$

with $V^{\perp, n+1/2}$ and $V^{z(1)} \equiv V^{z, n+1/2}$ to be $\mathcal{O}(\delta t^2)$ estimates at the intermediate time level $t^{n+1/2}$; see the subsequent Section 5. For the corrective iterations $\eta > 1$ the updated solution field Ψ is transported with the error-compensative pseudo-velocities which are of the functional dependency

$$V^{\perp(\eta+1)} = V^{\perp} \left(V^{\perp(\eta)}, V^{z(\eta)}, \check{\Psi}^{(\eta)}, G^n \right), \quad (22)$$

$$V^{z(\eta+1)} = V^z \left(V^{\perp(\eta)}, V^{z(\eta)}, \check{\Psi}^{(\eta)}, G^n \right), \quad (23)$$

$$\check{\Psi} \equiv \frac{G^n}{G^{n+1}} \Psi. \quad (24)$$

The weighted field $\check{\Psi}$ (24) in the pseudo-velocities (22) and (23) is crucial for the solution monotonicity under the time-dependent $G(\mathbf{x}, t)$ [18]. For $\mathcal{N}_\eta = 1$, the algorithm in (18)-(20) describes the first-order accurate upwind advection scheme. MPDATA achieves second-order accurate solutions with the subsequent corrective steps $\eta > 1$. Following the truncation error analysis above in Section 3, the novel error-compensative pseudo-velocities employed for $\eta > 1$ are formulated in the horizontal (22) as

$$V_{k,j}^{\perp(\eta+1)} = \frac{1}{2} |V_{k,j}^{\perp(\eta)}| \left(\frac{|\check{\Psi}_{k,j}^{(\eta)}| - |\check{\Psi}_{k,i}^{(\eta)}|}{|\check{\Psi}_k^{(\eta)}| + \epsilon} \right) - \frac{\delta t}{2} V_{k,j}^{\perp(\eta)} \frac{1}{G_k^{n ij}} \left(\frac{[\overline{\nabla \cdot (\mathbf{V}^{(\eta)} |\check{\Psi}^{(\eta)})}]_k^{ij}}{\langle |\check{\Psi}^{(\eta)}| \rangle_k + \epsilon} + \frac{\partial G_k}{\partial t} \right), \quad (25)$$

and in the vertical (23) as

$$V_{k+1/2,i}^{z(\eta+1)} = \frac{1}{2} |V_{k+1/2,i}^{z(\eta)}| \left(\frac{|\check{\Psi}_{k+1,i}^{(\eta)}| - |\check{\Psi}_{k,i}^{(\eta)}|}{|\check{\Psi}_i^{(\eta)}| + \epsilon} \right) - \frac{\delta t}{2} V_{k+1/2,i}^{z(\eta)} \frac{1}{G_i^{n k+1/2}} \left(\frac{[\overline{\nabla \cdot (\mathbf{V}^{(\eta)} |\check{\Psi}^{(\eta)})}]_i^{k+1/2}}{\langle |\check{\Psi}^{(\eta)}| \rangle_i + \epsilon} + \frac{\partial G_i}{\partial t} \right). \quad (26)$$

The horizontal pseudo-velocity expression (25) combines $\mathcal{O}(\delta r)$ and $\mathcal{O}(\delta t)$ truncation error compensations in the first and second term, respectively. The form of the $\mathcal{O}(\delta r)$ error is standard [3] and dispenses with a contribution from 'mesh skewness' that is zero for the considered median-dual discretisation; cf. Eq. (5). The pseudo-velocity (25) is defined at the dual cell face, and the overline operator combines the values from two neighbouring nodes i and j as $\overline{\phi}^{ij} = 0.5(\phi_i + \phi_j)$ for any scalar quantity ϕ . The vertical pseudo-velocity expression (26) similarly combines compensations for $\mathcal{O}(\delta z)$ and $\mathcal{O}(\delta t)$ truncation errors, and the values at the cell face are given as $\overline{\phi}^{k+1/2} = 0.5(\phi^k + \phi^{k+1})$; the expression for $V_{k-1/2,i}^z$ is defined analogously to $V_{k+1/2,i}^z$.

The $\mathcal{O}(\delta t)$ error terms in (25) and (26) derive from the modified equation (15). Here, the dominant contribution is from the generic flux divergence which we evaluate at node (k, i) as

$$[\nabla \cdot (\mathbf{V}\Psi)]_{k,i} = \frac{1}{V_i} \sum_{j=1}^{l(i)} C_{k,j}^{\perp} (\Psi_{k,i}, \Psi_{k,j}, V_{k,j}^{\perp}) S_j + \frac{1}{\delta z} \left\{ C_{k+1/2,i}^z (\Psi_{k+1,i}, \Psi_{k,i}, V_{k+1/2,i}^z) - C_{k-1/2,i}^z (\Psi_{k,i}, \Psi_{k-1,i}, V_{k-1/2,i}^z) \right\}, \quad (27)$$

with centred fluxes in the horizontal

$$C_{k,j}^\perp (\Psi_{k,i}, \Psi_{k,j}, V_{k,j}^\perp) = \frac{1}{2} V_{k,j}^\perp (\Psi_{k,i} + \Psi_{k,j}) \quad (28)$$

and in the vertical direction

$$C_{k+1/2,i}^z (\Psi_{k+1,i}, \Psi_{k,i}, V_{k+1/2,i}^z) = \frac{1}{2} V_{k+1/2,i}^z (\Psi_{k+1,i} + \Psi_{k,i}) , \quad (29)$$

again with $C_{k-1/2,i}^z$ defined analogously. The second contribution to the $\mathcal{O}(\delta t)$ term is independent of Ψ and can be precomputed at the nodes as

$$\frac{\partial G_{k,i}}{\partial t} = \frac{G_{k,i}^{n+1} - G_{k,i}^n}{\delta t} . \quad (30)$$

As in previous FD and FV formulations of MPDATA [5, 3, 20], normalisation of the truncation error expressions with $\sim \Psi$ is implemented such as to assure the boundedness of the pseudo-velocities (25) and (26), and hence the stability of the scheme. Given strictly nonnegative (or nonpositive) Ψ , this is achieved by constructing the normalisation in the denominator as a compound of the same elements as involved in the respective discrete operator of the numerator; it can be readily seen for the differencing $\Psi^{-1} \partial \Psi$ along the edges in the $\mathcal{O}(\delta r)$ error compensation terms of (25), respectively in the $\mathcal{O}(\delta z)$ terms of (26). Accordingly, we define $\langle \Psi \rangle$ in the denominator of the temporal $\mathcal{O}(\delta t)$ error compensation terms as an average of all Ψ 's involved in the discrete flux divergence operator $\nabla \cdot (\mathbf{V}\Psi)$. As the involved \mathbf{V}^η from the previous iteration is bounded, this ensures boundedness for the entire expression $\langle \Psi \rangle^{-1} \nabla \cdot (\mathbf{V}\Psi)$. Addition of the ϵ in the denominators, which denotes a small constant such as 10^{-10} , ensures validity of the formulae (25) and (26) when the Ψ 's become zero. The use of absolute values $|\Psi|$ in the pseudo-velocity expressions (25) and (26) conveniently extends stability and applicability of the scheme to fields Ψ of variable sign [5, 3]. The advanced scheme (16)-(30) naturally permits any number of error-compensative iterations $\mathcal{N}_\eta > 1$ on arbitrary meshes, but $\mathcal{N}_\eta \equiv 2$ in (18) suffices for second-order $\mathcal{O}(\delta r^2, \delta t^2)$ accuracy.

The described scheme is fully amenable to common MPDATA extensions addressed in Section 1. Most notably, these extensions include the nonoscillatory option that limits the pseudo-velocities to ensure monotone solutions [7, 3] and the infinite-gauge variant. The scheme (16)-(30) reduces to the two-pass (i.e. $\mathcal{N}_\eta \equiv 2$) infinite-gauge by replacing at the second iteration $\eta = 2$ the first two arguments of the upwind flux functions in (18) with unity, and the pseudo-velocity expressions (25) and (26) with

$$V_{k,j}^\perp{}^{(\eta+1)} = \frac{1}{2} |V_{k,j}^\perp{}^{(\eta)}| \left(\check{\Psi}_{k,j}^{(\eta)} - \check{\Psi}_{k,i}^{(\eta)} \right) - \frac{\delta t}{2} V_{k,j}^\perp{}^{(\eta)} \frac{1}{G_k^{n\,ij}} \left(\overline{[\nabla \cdot (\mathbf{V}^{(\eta)} \check{\Psi}^{(\eta)})]_k}{}^{-ij} + \overline{\check{\Psi}_k^{(\eta)}}{}^{ij} \frac{\partial G_k}{\partial t}{}^{ij} \right) \quad (31)$$

and

$$V_{k+1/2,i}^z{}^{(\eta+1)} = \frac{1}{2} |V_{k+1/2,i}^z{}^{(\eta)}| \left(\check{\Psi}_{k+1,i}^{(\eta)} - \check{\Psi}_{k,i}^{(\eta)} \right) - \frac{\delta t}{2} V_{k+1/2,i}^z{}^{(\eta)} \frac{1}{G_i^{n\,k+1/2}} \left(\overline{[\nabla \cdot (\mathbf{V}^{(\eta)} \check{\Psi}^{(\eta)})]_i}{}^{-k+1/2} + \overline{\check{\Psi}_i^{(\eta)}}{}^{k+1/2} \frac{\partial G_i}{\partial t}{}^{k+1/2} \right) . \quad (32)$$

5. Numerical integration of the compressible Euler equations for low Mach number flows

Following the formalism of [25, 33], the compressible Euler equations for inviscid, adiabatic, rotating stratified atmospheric flows are written as

$$\frac{\partial \mathcal{G} \rho}{\partial t} + \nabla \cdot (\mathbf{v} \mathcal{G} \rho) = 0 , \quad (33a)$$

$$\frac{\partial \mathcal{G} \rho \theta'}{\partial t} + \nabla \cdot (\mathbf{v} \mathcal{G} \rho \theta') = -\mathcal{G} \rho \tilde{\mathbf{G}}^T \mathbf{u} \cdot \nabla \theta_a , \quad (33b)$$

$$\frac{\partial \mathcal{G} \rho \mathbf{u}}{\partial t} + \nabla \cdot (\mathbf{v} \mathcal{G} \rho \mathbf{u}) = \mathcal{G} \rho \left(-\frac{\theta}{\theta_0} \tilde{\mathbf{G}} \nabla \varphi - \mathbf{g} \frac{\theta'}{\theta_a} - \mathbf{f} \times \left(\mathbf{u} - \frac{\theta}{\theta_a} \mathbf{u}_a \right) + \mathcal{M}'(\mathbf{u}, \mathbf{u}_a, \theta/\theta_a) \right), \quad (33c)$$

which describe the conservation laws of mass, entropy and momentum, respectively. Dependent variables in (33) are density ρ , potential temperature perturbation θ' , three-dimensional physical velocity vector \mathbf{u} , and $\varphi := c_p \theta_0 \pi'$ where π' is the Exner pressure perturbation. The perturbations (indicated by the primes) are with respect to a balanced ambient state (denoted by subscript "a") [19, 25]. The subscript "0" appearing with θ_0 and the pressure p_0 below in (34) refers to constant reference values, whereas c_p is the specific heat at constant pressure. On the rhs of the momentum equation (33c) is the gravity vector $\mathbf{g} \equiv (0, 0, -g)$, the Coriolis parameter \mathbf{f} , and \mathcal{M}' subsumes the metric forces due to the curvature of the sphere; see Appendix A of [33] for the explicit expressions. Furthermore, the governing equations (33) are formulated with respect to a geospherical coordinate system and a generalised terrain-following vertical coordinate which may optionally be time-dependent. Associated symbols are the transformed curvilinear coordinates \mathbf{x} , the 3D nabla operator ∇ with respect to \mathbf{x} , the Jacobian \mathcal{G} of the coordinate transformations (i.e. the square root of the determinant of the metric tensor), a matrix of metric coefficients $\tilde{\mathbf{G}}$, its transpose $\tilde{\mathbf{G}}^T$, and the contravariant velocity $\mathbf{v} = \dot{\mathbf{x}} = \tilde{\mathbf{G}}^T \mathbf{u} + \mathbf{v}^g$ where $\mathbf{v}^g \equiv \partial \mathbf{x} / \partial t$ is the mesh velocity; see [17, 18] for discussion.

In [25], the authors described several two-time-level integration approaches for the compressible Euler equations (33). These approaches include explicit acoustic integration where the thermodynamic pressure is computed straightforwardly using the ideal gas law

$$\varphi = c_p \theta_0 \left[\left(\frac{R_d}{p_0} \rho \theta \right)^{R_d/c_v} - \pi_a \right], \quad (34)$$

with R_d and c_v symbolising the gas constant and the specific heat at constant volume, respectively. More relevant though are the efficient large-time-step semi-implicit integrators that provide unconditional stability with respect to fast buoyant and acoustic modes described further below. In either approach of [25], two-time-level integration of the compressible Euler equations (33) commences with the mass continuity equation (33a) as

$$\rho_{\mathbf{i}}^{n+1} = \mathcal{A}_{\mathbf{i}} \left(\rho^n, (\mathbf{v} \mathcal{G})^{n+1/2}, \mathcal{G}^n, \mathcal{G}^{n+1} \right), \quad (35)$$

where the operator $\mathcal{A}_{\mathbf{i}}$ symbolises the MPDATA advection scheme (16). Arguments of $\mathcal{A}_{\mathbf{i}}$ in (35) are the density ρ^n , the advector $(\mathbf{v} \mathcal{G})^{n+1/2}$, and the Jacobian \mathcal{G} at t^n and t^{n+1} . Given the provision of a first-order accurate estimate of the advector $(\mathbf{v} \mathcal{G})^{n+1/2}$ at the intermediate time level $t^{n+1/2}$,² $\mathcal{A}_{\mathbf{i}}$ provides a second-order accurate solution for ρ^{n+1} at the spatial position $\mathbf{x}_{\mathbf{i}}$. In addition to updating ρ , the scheme (35) also accumulates the face-normal advective mass fluxes $(v^\perp \mathcal{G} \rho)^{n+1/2}$ in 3D employed in the computation of the discrete mass flux divergence in (18). These advective mass fluxes and the updated density ρ^{n+1} are subsequently applied in the integration of all other model conservation laws.

Denoting each of the other dependent variables as $\Psi = \theta', u, v, w$ and subsuming the respective rhs forcing terms as \mathcal{R}^Ψ , each of the governing equations (33b)-(33c) can compactly be written as

$$\frac{\partial \mathcal{G} \rho \Psi}{\partial t} + \nabla \cdot (\mathbf{v} \mathcal{G} \rho \Psi) = \mathcal{G} \rho \mathcal{R}^\Psi. \quad (36)$$

Referring to the modified equation analysis of Section 3, a two-time-level fully second-order-accurate semi-implicit integration scheme for the generic conservation law (36) is given as

$$\Psi_{\mathbf{i}}^{n+1} = \mathcal{A}_{\mathbf{i}} \left(\tilde{\Psi}^n, (v^\perp \mathcal{G} \rho)^{n+1/2}, (\mathcal{G} \rho)^n, (\mathcal{G} \rho)^{n+1} \right) + 0.5 \delta t \mathcal{R}^\Psi|_{\mathbf{i}}^{n+1} \equiv \hat{\Psi}_{\mathbf{i}} + 0.5 \delta t \mathcal{R}^\Psi|_{\mathbf{i}}^{n+1} \quad (37)$$

²Standardly, to obtain $(\mathbf{v} \mathcal{G})^{n+1/2}$ we use linear extrapolation of $\mathbf{v} \mathcal{G}$ from the t^{n-1} and t^n time levels; see [18] for a description that also accounts for time-dependent (i.e. moving) curvilinear coordinates.

where advection of the auxiliary field $\tilde{\Psi}^n \equiv \Psi^n + 0.5 \delta t \mathcal{R}^\Psi |^n$ compensates for the $\mathcal{O}(\delta t)$ error proportional to the rhs R^Ψ in (13) and (15) [4]. The operator \mathcal{A} in (37) assumes the advector defined by the face-normal mass fluxes $(v^\perp \mathcal{G} \rho)^{n+1/2}$ accumulated in the integration of the mass continuity (35), along with $(\mathcal{G} \rho)^n$ and $(\mathcal{G} \rho)^{n+1}$, thereby ensuring full compatibility with mass continuity.

The integration of the compressible equations (33) proceeds by substituting the scheme (37) for θ' into the buoyancy term of the scheme (37) for \mathbf{u} , and inverting the overall discrete system³. This results in a closed-form expression for the velocity update \mathbf{u} on the rhs of which the pressure gradient term is retained. Omitting spatial and temporal indices, the latter can compactly be written as

$$\mathbf{u} = \mathbf{L}^{-1} \left[\widehat{\mathbf{u}} \left(\widehat{\mathbf{u}}, \widehat{\theta}', \mathbf{u}^*, \theta^* \right) - 0.5 \delta t \frac{\theta^*}{\theta_0} \tilde{\mathbf{G}} \nabla \varphi \right] \equiv \check{\mathbf{u}} - \mathbf{C} \nabla \varphi, \quad (38)$$

where $\widehat{\mathbf{u}}$ represents the explicit part depending on contributions from advection and the other nonlinear terms which are lagged behind and executed in an outer iteration (the variables associated with the nonlinear terms are denoted by the superscript \star), while \mathbf{L} indicates the linear operator acting on \mathbf{u} .

The large-time-step enhancement for low Mach number flows continues with formulation of a 3D implicit boundary value problem for the pressure variable φ [25]. The employed constraint derives from the evolutionary form of the equation of state (34), leading to

$$\frac{\partial \mathcal{G} \rho \varphi}{\partial t} + \nabla \cdot (\mathbf{v} \mathcal{G} \rho \varphi) = \mathcal{G} \rho \left(-\frac{R_d}{c_v} \frac{\phi}{\mathcal{G}} \nabla \cdot (\mathcal{G} \tilde{\mathbf{G}}^T \mathbf{u}) - \frac{1}{\mathcal{G} \rho} \nabla \cdot (\mathcal{G} \rho \tilde{\mathbf{G}}^T \mathbf{u} \phi_a) + \frac{\phi_a}{\mathcal{G} \rho} \nabla \cdot (\mathcal{G} \rho \tilde{\mathbf{G}}^T \mathbf{u}) \right) \equiv \mathcal{G} \rho \mathcal{R}^\varphi, \quad (39)$$

where $\phi_a \equiv c_p \theta_0 \pi_a$ and $\phi \equiv \phi_a + \varphi$. An $\mathcal{O}(\delta t^2)$ integration of (39) with an Euler backward scheme in the spirit of (37) is given as

$$\varphi_{\mathbf{i}}^{n+1} = \mathcal{A}_{\mathbf{i}} \left(\varphi^n, (v^\perp \mathcal{G} \rho)^{n+1/2}, (\mathcal{G} \rho)^n, (\mathcal{G} \rho)^{n+1} \right) + \delta t \mathcal{R}^\varphi |_{\mathbf{i}}^{n+1} \equiv \widehat{\varphi}_{\mathbf{i}} + \delta t \mathcal{R}^\varphi |_{\mathbf{i}}^{n+1}, \quad (40)$$

which upon elimination of (38) yields the elliptic Helmholtz equation [25, 33]

$$0 = - \sum_{\ell=1}^3 \left(\frac{A_\ell^*}{\zeta_\ell} \nabla \cdot \zeta_\ell \tilde{\mathbf{G}}^T (\check{\mathbf{u}} - \mathbf{C} \nabla \varphi) \right) - B^*(\varphi - \widehat{\varphi}). \quad (41)$$

The summation in (41) is over the three divergence operators of the implicit forcing \mathcal{R}^φ on the rhs of (39), respectively (40), while the coefficients A^* , B^* and ζ_ℓ are defined accordingly. The 3D boundary value problem (41) is solved iteratively using a bespoke preconditioned Generalised Conjugate Residual approach; see [28] for a recent discussion and [36, 37] for tutorials. The dependence of the coefficients A^* and B^* on φ in (41) is again lagged behind. The reader is referred to [25, 33] for further details about the integration procedure.

The developments of [25] focused on atmospheric flow simulations with rectilinear computational grids. If the mesh becomes non-rectilinear, MPDATA based on the modified equation (13) lacks the face-tangential velocity required to specify the advective term $\sim \mathbf{V} \cdot \nabla \Psi$, as only the face-normal vector components $(v^\perp \mathcal{G} \rho)^{n+1/2}$ are provided in (37) and (40) compatible with the discrete mass continuity (35). Therefore, the alternative FV-MPDATA developed in the present work is important to extend the large-time-step semi-implicit integration for the compressible Euler equations of [25] from rectilinear to arbitrary hybrid meshes.

Notably, the current MPDATA advancement is not required with the semi-implicit integration schemes for soundproof (anelastic, pseudo-incompressible) equations [3, 28, 12, 25, 13, 33]. Soundproof equations use a reduced diagnostic form of the mass continuity $\nabla \cdot (\mathcal{G} \rho \tilde{\mathbf{G}}^T \mathbf{u}) = 0$ where ρ is a prescribed time-independent density. Consequently, this obviates the integration of the prognostic mass continuity equation and reduces the computation of the MPDATA advector to a soundproof predictor, typically linear extrapolation of \mathbf{v} from t^{n-1} and t^n to obtain $(\mathbf{v} \mathcal{G} \rho)^{n+1/2}$, which then enters in (37). As the extrapolated mass flux $(\mathbf{v} \mathcal{G} \rho)^{n+1/2}$ involves the full velocity vector \mathbf{v} , in contrast to only the face-normal component v^\perp , the FV-MPDATA based on the classical form (13), also (5), is by itself completely specified for arbitrary meshes.

³Inversion is facilitated by the colocated arrangement of all variables and coefficients.

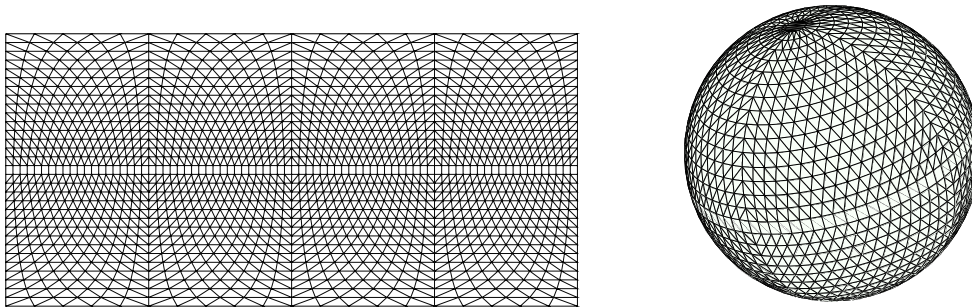


Fig. 2: The employed primary mesh associated with the octahedral reduced Gaussian grid in computational (left) and physical (right) space, illustrated here using 16 latitudes between pole and equator ('O16').

6. Results of numerical simulations

We validate the advanced FV-MPDATA by means of comparison to reference solutions. First we compare the scheme to the established FV-MPDATA formulation for the integration of soundproof equations common in small- and mesoscale dynamics [28, 29]. This comparison is conducted in Section 6.1 for a mesoscale mountain wave using the small planet configuration. Section 6.2 applies the semi-implicit scheme for the compressible Euler equations using the advanced FV-MPDATA to reproduce reference solutions of a global baroclinic instability benchmark on a real-sized planet.

All numerical simulations use the median-dual FV mesh developed about the nodes of the octahedral reduced Gaussian grid [33]. The associated primary mesh is composed of triangular and quadrilateral elements as illustrated in Fig. 2—the dual mesh associated with this primary mesh consists of general polygons (not shown). The octahedral reduced Gaussian grid provides quasi-uniform resolution over the spherical surface in physical space⁴.

6.1. Mesoscale mountain waves

We consider the problem of orographically-forced internal gravity waves in an atmosphere with vertical wind shear [38]. Because we are concerned with global atmospheric modelling, we use the small-planet configuration where the radius of the spherical Earth is reduced in order to achieve nonhydrostatic resolutions at relatively low computational cost [39]. In the specification of the setup we closely follow [33] but specify the radius of the spherical planet to $r_0 = 40$ km. A three-dimensional hill with a maximum height of $h_0 = 500$ m, an elliptical horizontal cross section and the classical "witch of Agnesi" vertical profile is centred at the equator. The associated surface height field as a function of latitude ϕ and longitude λ is given as

$$h(\phi, \lambda) = h_0 \left(1 + l_\lambda^2/L_\lambda^2 + l_\phi^2/L_\phi^2 \right)^{-1}, \quad (42)$$

with $l_\lambda = r_0 \cos^{-1}[\sin^2(\phi_c) + \cos^2(\phi_c) \cos(\lambda - \lambda_c)]$ and $l_\phi = r_0 \cos^{-1}[\sin \phi_c \sin \phi + \cos \phi_c \cos \phi]$, where the mountain half-width is $L_\lambda = 2.5$ km, and the meridional extent of the ellipse is defined by $L_\phi = |L_\lambda^2 - L_f^2|^{1/2}$. The centre position of the mountain is $(\lambda_c, \phi_c) = (3\pi/2, 0)$, and the focus point distance is $L_f = r_0 \cos^{-1}[\sin \phi_d \sin \phi_c + \cos \phi_d \cos \phi_c \cos(\lambda_d - \lambda_c)]$ with $(\lambda_d, \phi_d) = (3\pi/2, \pi/3)$. Ambient flow conditions describe a linearly sheared zonal wind profile $(u_a, v_a, w_a) = (U_0(1 + Cz) \cos \phi, 0, 0)$ below the tropopause located at a height of 10.5 km and a constant zonal wind $(u_a, v_a, w_a) = (U_0, 0, 0)$ above, where $U_0 = 10 \text{ m s}^{-1}$, $C = 2.5 \times 10^{-4} \text{ m}^{-1}$. An isothermal ambient state with $T_0 = g^2/(c_p N^2)$ and constant stability $N = 0.01 \text{ ms}^{-1}$ defines the thermodynamic structure of the atmosphere. For the applied small planet

⁴The octahedral reduced Gaussian grid is also suitable for spherical harmonics transforms applied in spectral numerical weather prediction models, and using a common unified grid facilitates interoperability of the different numerical solution approaches in future forecasting systems [33].

Simulation	Equations	FV-MPDATA
PI-ADV	pseudo-incompressible	established form based on Eq. (13)
PI-DIV	pseudo-incompressible	advanced form based on Eq. (15)
CMP-DIV	compressible Euler	advanced form based on Eq. (15)

Table 1: Summary of the three different model configurations used to validate the proposed FV-MPDATA. Two different governing equations—pseudo-incompressible (soundproof) equations or compressible Euler equations—solved by the respective large-time-step integration schemes with either the established or advanced FV-MPDATA formulations.

	PI-ADV	PI-DIV	CMP-DIV
L_2	0.0	$2.24 \cdot 10^{-7}$	$1.63 \cdot 10^{-6}$
L_{inf}	0.0	$6.98 \cdot 10^{-3}$	$2.69 \cdot 10^{-2}$

Table 2: Mountain-wave simulation after 2 h: Global L_2 and L_{inf} error norms in terms of the vertical velocity difference (m s^{-1}) between the reference PI-ADV and all other model configurations in Table 1.

configuration, the governing equations assume the shallow-atmosphere approximation and the planetary rotation is set to zero.

The simulations were performed with the computational mesh developed about the nodes of the octahedral reduced Gaussian grid of size O90, cf. Fig. 2, which results in a quasi-uniform horizontal mesh spacing of about 700 m. This was combined with 60 model levels in the vertical, stretched from a minimum spacing of 110 m near the ground to 2250 m to the model top located 59 km. The time step was continuously adapted such that the maximum advective Courant number is 0.95—the average time step over the 2 h simulations was about 8.5 s. Three different model configurations summarised in Table 1 were used to validate the advanced FV-MPDATA against the reference given by the established FV-MPDATA. All results were obtained with the nonoscillatory infinite-gauge variant of MPDATA. No explicit diffusion or filtering was employed.

Figure 3 shows horizontal and vertical cross sections of vertical velocity after 2 h of simulation. Results produce the correct nonhydrostatic flow solution of a trapped, horizontally-propagating gravity wave with wavelength ≈ 14 km (20° of longitude) in the lee of the hill—this trapped wave is characteristic of the sheared ambient flow [38]. Some wave energy also propagates vertically through the tropopause, resulting in a weaker stratospheric wave of a longer wavelength. Solutions for the two different model configurations shown in Fig. 3, the reference PI-ADV and newly proposed CMP-DIV, are essentially indistinguishable. This is corroborated by the complementary Fig. 4, which directly aligns the solutions of all model configurations given in Table 1 by means of the vertical velocity along the centreline of the trapped lee wave. Together with the difference norms to the reference shown in Table 2, the results demonstrate that the advanced FV-MPDATA for both pseudo-incompressible (PI-DIV) and the compressible Euler equations (CMP-DIV) maintains fully the accuracy of the established FV-MPDATA for pseudo-incompressible equations (PI-ADV). The runtime difference between the PI-DIV and PI-ADV (i.e. both solving the pseudo-incompressible equations) for the 2 h simulation was below 0.3%, thus the cost of the established and advanced FV-MPDATA can be considered identical.

6.2. Global baroclinic instability benchmark

We further verify our MPDATA advancement using a global baroclinic instability benchmark problem, and follow the setup as described in the 2016 edition of DCMIP (Dynamical Core Model Intercomparison Project) [40]. The baroclinic instability benchmark problem resembles the evolution of natural weather systems in the mid-latitudes of the global atmosphere. As the emphasis in the present paper is on the basic numerical advancements we focus on a dry adiabatic flow. The adopted setup defines two mid-latitude zonal

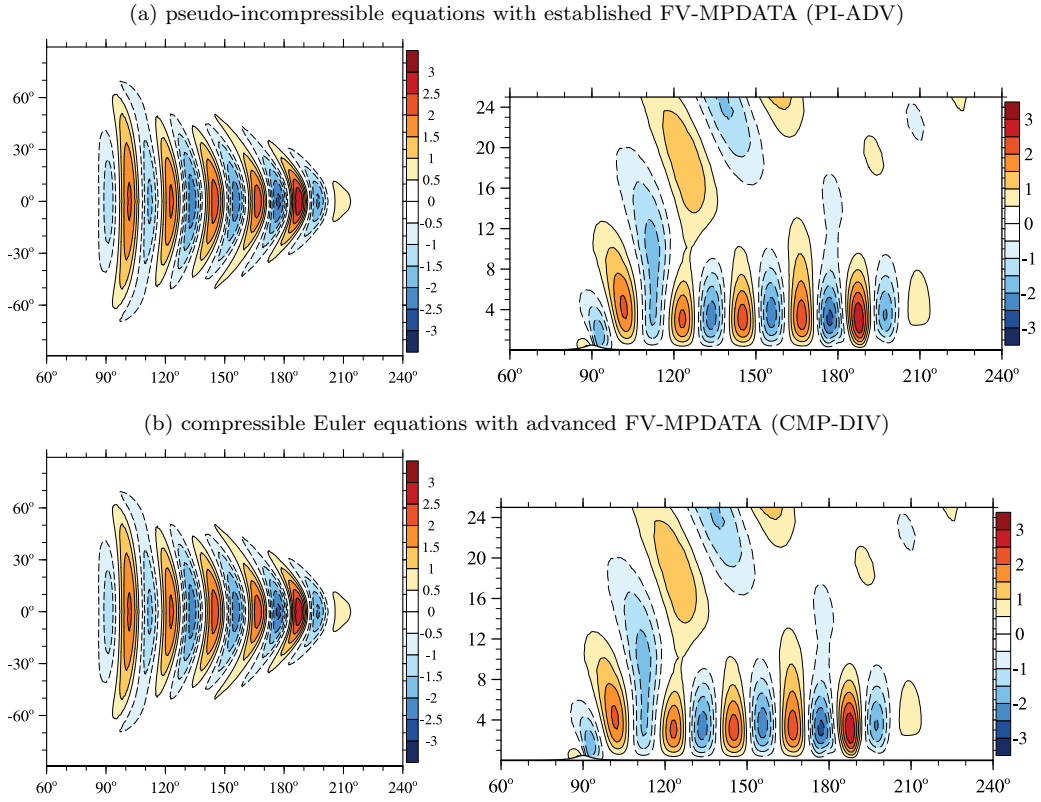


Fig. 3: Mountain-wave simulation after 2 h: vertical velocity w (m s^{-1}) in a horizontal cross section $[60^\circ, 240^\circ] \times [-90^\circ, 90^\circ]$ at height 3.5 km (left panel) and in zonal-height cross section $[60^\circ, 240^\circ] \times [0, 25 \text{ km}]$ along the equator (right panel) for model configurations (a) PI-ADV and (b) CMP-DIV given in Table 1. The simulations were performed with the O90 mesh, cf. Fig. 2, which corresponds to a grid spacing of 1° along the equator.

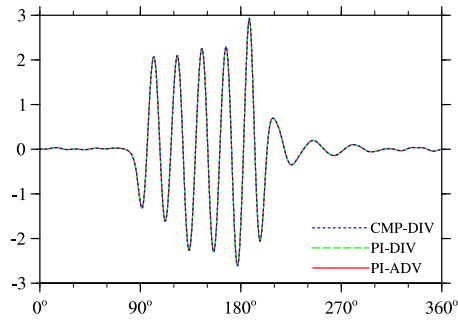


Fig. 4: Mountain-wave simulation after 2 h: vertical velocity w (m s^{-1}) along the equatorial line $[0^\circ, 360^\circ]$ at height 3.5 km, proceeding through the centreline of the trapped lee wave depicted in Fig. 3. Results are for the three different model configurations in Table 1.

jets, in thermal wind balance with the meridional temperature distribution, which are symmetric about the equator [41]. Here, the setup and model consistently assume the deep-atmosphere compressible Euler equations. A local zonal velocity perturbation in the form of a simple exponential bell (tapered to zero in the vertical) excites the instability, leading to eastward propagating Rossby modes. After about 15 days of integration, the flow in the region of the northerly jet becomes turbulent. We show simulation results at day 10, when the baroclinic wave has broken and formed sharp fronts in the lower troposphere. Furthermore, we present kinetic energy spectra deep in the turbulent flow stage at day 30.

All simulations were performed with the large-time-step semi-implicit integration scheme for the compressible Euler equations using the advanced FV-MPDATA—the corresponding model configuration in Table 1 is CMP-DIV. Again, results were obtained with the nonoscillatory infinite-gauge variant of MPDATA. Here, results are mainly discussed for the O180 octahedral reduced Gaussian grid, which corresponds to quasi-uniform mesh spacing of about 55 km, but we also applied larger grid sizes of up to O720 for the analysis of kinetic energy spectra. The vertical mesh consisted of 30 stretched levels, where the spacing varied from a minimum of 120 m near the surface to 2250 m near the model top located at 30 km. The variable time step targeted the maximum advective Courant number 0.95—the time step for the O180 grid varied from 1200 s during the first 7 days to somewhat under 200 s towards the end of the 30 day simulation. Again, no explicit diffusion or filtering was employed.

Figure 5 depicts the fields of surface pressure, as well as both temperature and relative vorticity on the 850 hPa pressure surface ⁵. The vertical structure of the baroclinic wave is revealed by Fig. 6 that displays the pressure perturbation from the initial pressure distribution at the same time as Fig. 5. Overall, the simulation results depict the common structure of idealised cyclo- and frontogenesis. Figure 7 provides instantaneous surface kinetic energy spectra after 30 days of simulation, for various octahedral grid sizes from O90 to O720. The spectra indicate the effective resolution relative to the grid spacing, and highlight the ILES property of MPDATA near the grid scale.

7. Conclusions

The proposed advancement of the finite-volume MPDATA enables large-time-step semi-implicit integration of the compressible Euler equations on arbitrary hybrid computational meshes. This scheme is important for the prediction of high-Reynolds low-Mach number global atmospheric flows. The key aspect of the MPDATA advancement is to use freedom in the underlying forward-in-time truncation error analysis to formulate the error-compensative pseudo-velocity such that it operates solely on face-normal vector components to the dual cells, consistent with the flux-divergence of the governing conservation law. This is in contrast to previous MPDATA formulations which require the full velocity vector including face-tangential components to specify the pseudo-velocity. The resulting finite-volume MPDATA achieves full compatibility with the discrete finite-volume representation of the compressible mass continuity which is imperative for high solution quality. Another virtue, independent of the integration of the compressible Euler equations, is the straightforward option of multiple error-compensative iterations on arbitrary meshes.

Discrete implementations of the advanced finite-volume MPDATA were presented in a hybrid horizontally-unstructured vertically-structured computational mesh formulation bespoke to 3D atmospheric dynamics in thin spherical (or spheroidal) shells—the discrete formulae for fully unstructured meshes in 3D are obtained simply by neglecting in the given expressions the index pertaining to the structured vertical discretisation. In addition to the complexities associated with the horizontally-unstructured vertically-structured mesh formulation, the presented finite-volume scheme rigorously accounts for (optionally time-dependent) curvilinear coordinates.

Numerical simulations of 3D atmospheric flows in hydrostatic and nonhydrostatic regimes confirmed the efficacy of the proposed finite-volume MPDATA on unstructured meshes. First, the scheme fully retains the accuracy and efficiency of established finite-volume MPDATA formulations in the context of soundproof

⁵The relative vorticity on the 850 hPa pressure surface is obtained by computing the relative vorticity on model levels (consistent with the model metrics [42]) followed by linear interpolation to the pressure level.

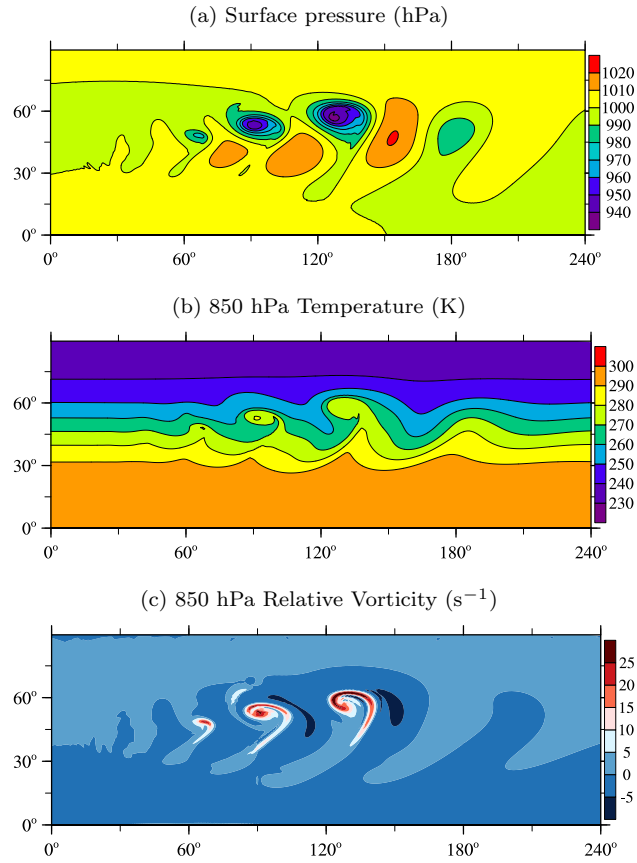


Fig. 5: Baroclinic instability benchmark at day 10: Horizontal cross sections $[0^\circ, 240^\circ] \times [0^\circ, 90^\circ]$ of surface pressure (hPa), 850 hPa temperature (K), and 850 hPa relative vorticity (s^{-1}). Results are from the large-time-step semi-implicit integration of the compressible Euler equations with the advanced FV-MPDATA on the O180 grid.

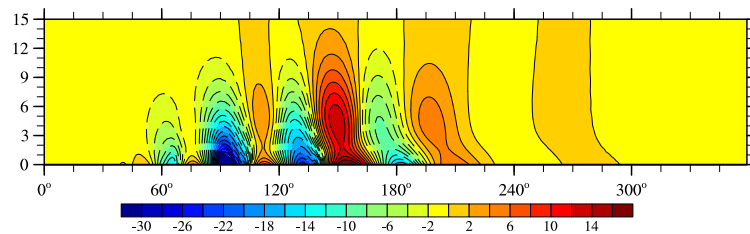


Fig. 6: Baroclinic instability benchmark at day 10 as in Fig. 5: pressure perturbation from the initial state (hPa) in a zonal-height cross section $[0^\circ, 360^\circ] \times [0, 15 \text{ km}]$ at 50° N .

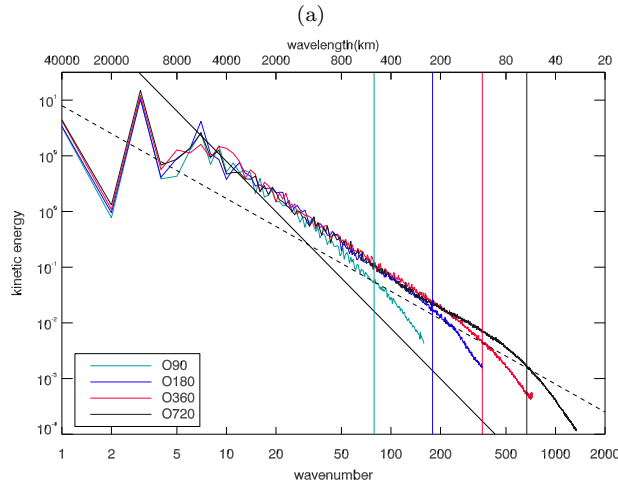


Fig. 7: Baroclinic instability benchmark: Surface kinetic energy spectra at day 30, simulated with various resolutions of the median-dual FV mesh developed about the nodes of the octahedral reduced Gaussian grid. Vertical lines in the corresponding colour indicate four grid intervals for the various resolutions. The -3 and $-5/3$ slopes are shown with solid and dashes lines, respectively.

equations. Second, when extended to the semi-implicit integration of the compressible Euler equations the scheme reproduces the reference results of soundproof equations and also compares favourably with global atmospheric flow benchmark solutions. The presented scheme is used as a default for the semi-implicit integration of soundproof and compressible Euler equations in the finite-volume module (FVM) for global all-scale atmospheric flows [33].

Acknowledgements: We gratefully acknowledge comments by two reviewers. This work was supported in part by funding received from the European Research Council under the European Union’s Seventh Framework Programme (FP7/2012/ERC Grant agreement no. 320375).

References

- [1] P. Bauer, A. Thorpe, G. Brunet, The quiet revolution of numerical weather prediction, *Nature* 525 (2015) 47–55.
- [2] P. K. Smolarkiewicz, A fully multidimensional positive definite advection transport algorithm with small implicit diffusion, *J. Comput. Phys.* 54 (1984) 325–362.
- [3] P. K. Smolarkiewicz, J. Szmelter, MPDATA: an edge-based unstructured-grid formulation, *J. Comput. Phys.* 206 (2005) 624–649.
- [4] P. K. Smolarkiewicz, L. G. Margolin, On forward-in-time differencing for fluids - Extension to a curvilinear framework, *Mon. Wea. Rev.* 121 (1993) 1847–1859.
- [5] P. K. Smolarkiewicz, L. G. Margolin, MPDATA: a finite-difference solver for geophysical flows, *J. Comput. Phys.* 140 (1998) 459–480.
- [6] P. K. Smolarkiewicz, Multidimensional positive definite advection transport algorithm: An overview, *Int. J. Numer. Meth. Fluids* 50 (2006) 1123–1144.
- [7] P. K. Smolarkiewicz, W. Grabowski, The multidimensional positive definite advection transport algorithm: nonoscillatory option, *J. Comput. Phys.* 86 (1990) 355–375.
- [8] P. K. Smolarkiewicz, T. L. Clark, The multidimensional positive definite advection transport algorithm: further development and applications, *J. Comput. Phys.* 67 (1986) 396–438.
- [9] J. A. Domaradzki, Z. Xiao, P. K. Smolarkiewicz, Effective eddy viscosities in implicit large eddy simulations of turbulent flows, *Physics of Fluids* 15 (2003) 3890–3893.
- [10] L. G. Margolin, W. J. Rider, F. F. Grinstein, Modeling turbulent flow with implicit LES, *J. Turbul.* 7 (2006) 1–27.
- [11] Z. P. Piotrowski, P. K. Smolarkiewicz, S. P. Malinowski, A. A. Wyszogrodzki, On numerical realizability of thermal convection, *J. Comp. Phys.* 228 (2009) 6268–6290.
- [12] P. K. Smolarkiewicz, J. Szmelter, A. A. Wyszogrodzki, An unstructured-mesh atmospheric model for nonhydrostatic dynamics, *J. Comput. Phys.* 254 (2013) 184–199.

- [13] J. Szmelter, Z. Zhang, P. K. Smolarkiewicz, An unstructured-mesh atmospheric model for nonhydrostatic dynamics: Towards optimal mesh resolution, *J. Comput. Phys.* 294 (2015) 363–381.
- [14] A. L. Marsden, O. V. Vasilyev, P. Moin, Construction of commutative filters for LES on unstructured meshes, *J. Comput. Phys.* 175 (2002) 584–603.
- [15] J. M. Prusa, P. K. Smolarkiewicz, R. R. Garcia, Propagation and breaking at high altitudes of gravity waves excited by tropospheric forcing, *J. Atmos. Sci.* 53 (1996) 2186–2216.
- [16] N. P. Wedi, P. K. Smolarkiewicz, Extending Gal-Chen and Somerville terrain-following coordinate transformation on time-dependent curvilinear boundaries, *J. Comput. Phys.* 193 (2004) 1–20.
- [17] J. M. Prusa, P. K. Smolarkiewicz, An all-scale anelastic model for geophysical flows: dynamic grid deformation, *J. Comput. Phys.* 190 (2003) 601–622.
- [18] C. Kühnlein, P. K. Smolarkiewicz, A. Dörnbrack, Modelling atmospheric flows with adaptive moving meshes, *J. Comput. Phys.* 231 (2012) 2741–2763.
- [19] J. M. Prusa, P. K. Smolarkiewicz, A. A. Wyszogrodzki, EULAG, a computational model for multiscale flows, *Comput. Fluids* 37 (2008) 1193–1207.
- [20] P. K. Smolarkiewicz, J. Szmelter, Multidimensional positive definite advection transport algorithm (MPDATA): an edge-based unstructured-data formulation, *Int. J. Numer. Meth. Fluids* 47 (2005) 1293–1299.
- [21] J. Szmelter, P. K. Smolarkiewicz, MPDATA error estimator for mesh adaptivity, *Int. J. Numer. Meth. Fluids* 50 (2006) 1269–1293.
- [22] J. Szmelter, P. K. Smolarkiewicz, An edge-based unstructured mesh discretisation in geospherical framework, *J. Comput. Phys.* 229 (2010) 4980–4995.
- [23] J. D. Hyman, P. K. Smolarkiewicz, C. L. Winter, Heterogeneities of flow in stochastically generated porous media, *Phys. Rev. E* 86.
- [24] M. Ghizaru, P. Charbonneau, P. K. Smolarkiewicz, Magnetic Cycles in Global Large-eddy Simulations of Solar Convection, *Astrophys. J. Lett.* 715 (2010) L133–L137.
- [25] P. K. Smolarkiewicz, C. Kühnlein, N. P. Wedi, A consistent framework for discrete integrations of soundproof and compressible PDEs of atmospheric dynamics, *J. Comput. Phys.* 263 (2014) 185–205.
- [26] P. K. Smolarkiewicz, J. Szmelter, Iterated upwind schemes for gas dynamics, *J. Comput. Phys.* 228 (2009) 33–54.
- [27] P. K. Smolarkiewicz, A. Dörnbrack, Conservative integrals of adiabatic Durran’s equations, *Int. J. Numer. Meth. Fluids* 56 (2008) 1513–1519.
- [28] P. Smolarkiewicz, J. Szmelter, A nonhydrostatic unstructured-mesh soundproof model for simulation of internal gravity waves, *Acta Geophys.* 59 (2011) 1109–1134.
- [29] J. Szmelter, P. Smolarkiewicz, An edge-based unstructured mesh framework for atmospheric flows, *Comput. Fluids* 46 (2011) 455–460.
- [30] A. Dörnbrack, J. D. Doyle, T. P. Lane, R. D. Sharman, P. K. Smolarkiewicz, On physical realizability and uncertainty of numerical solutions, *Atmosph. Sci. Lett.* 6 (2005) 118–122.
- [31] D. Jarecka, A. Jaruga, P. K. Smolarkiewicz, A spreading drop of shallow water, *J. Comput. Phys.* 289 (2015) 53–61.
- [32] D. P. Bacon, N. N. Ahmad, Z. Boybeyi, T. J. Dunn, M. S. Hall, P. C. S. Lee, R. A. Sarma, M. D. Turner, K. T. Waight, S. H. Young, J. W. Zack, A dynamically adapting weather and dispersion model: the operational multiscale environment model with grid adaptivity (OMEGA), *Mon. Wea. Rev.* 128 (2000) 2044–2076.
- [33] P. K. Smolarkiewicz, W. Deconinck, M. Hamrud, C. Kühnlein, G. Mozdzyński, J. Szmelter, N. P. Wedi, A finite-volume module for simulating global all-scale atmospheric flows, *J. Comput. Phys.* 314 (2016) 287–304.
- [34] E. Toro, *Riemann solvers and numerical methods for fluid dynamics: A practical introduction*, Springer, 2010.
- [35] P. K. Smolarkiewicz, J. Szmelter, F. Xiao, Simulation of all-scale atmospheric dynamics on unstructured meshes, *J. Comput. Phys.* 322 (2016) 267–287.
- [36] P. K. Smolarkiewicz, L. Margolin, Variational methods for elliptic problems in fluid models, In: *ECMWF Proceedings, Workshop on developments in numerical methods for very high resolution global models*. Reading, UK (2000) 137–159.
- [37] P. K. Smolarkiewicz, C. Temperton, S. J. Thomas, A. A. Wyszogrodzki, Spectral Preconditioners for nonhydrostatic atmospheric models: extreme applications, In: *Proceedings of the ECMWF seminar series on recent developments in numerical methods for atmospheric and ocean modelling*. Reading, UK (2004) 203–220.
- [38] T. L. Keller, Implications of the hydrostatic assumption on atmospheric gravity waves, *J. Atmos. Sci.* 51 (1994) 1915–1929.
- [39] N. P. Wedi, P. K. Smolarkiewicz, A framework for testing global non-hydrostatic models, *Q. J. Roy. Meteorol. Soc.* 135 (2009) 469–484.
- [40] P. A. Ullrich, C. Jablonowski, K. A. Reed, C. Zarzycki, P. H. Lauritzen, R. D. Nair, J. Kent, A. Verlet-Banide, Dynamical Core Model Intercomparison Project (DCMIP2016) Test Case Document. URL <https://github.com/ClimateGlobalChange/DCMIP2016>
- [41] P. A. Ullrich, T. Melvin, C. Jablonowski, A. Staniforth, A proposed baroclinic wave test case for deep- and shallow-atmosphere dynamical cores, *Q. J. Roy. Meteorol. Soc.* 140 (2014) 1590–1602.
- [42] P. K. Smolarkiewicz, J. M. Prusa, Towards mesh adaptivity for geophysical turbulence: continuous mapping approach, *Int. J. Numer. Meth. Fluids* 47 (2005) 789–801.